Development of Highly Efficient CuIn0.5Ga0.5Se2-based Photocathode and Application to Overall Solar Driven Water Splitting

Journal Name

ROYAL SOCIETY
OF CHEMISTRY

ARTICLE

Development of Highly Efficient CuIn$_{0.5}$Ga$_{0.5}$Se$_2$-based Photocathode and Application to Overall Solar Driven Water Splitting

Hiroyuki Kobayashi[a,b,d], Naotoshi Sato[a,b,d], Masahiro Orita[d], Yongbo Kuang[a,d], Hiroyuki Kaneko[a], Tsutomu Minegishi[a,c,d], Taro Yamada[a,d], and Kazunari Domen[a,d*]

A CuIn$_{1-x}$Ga$_x$Se$_2$ (CIGS) photocathode having a specific composition exhibited remarkable promotion of hydrogen evolution from water, with a half-cell solar-to-hydrogen conversion efficiency of 12.5%. CIGS thin films with various compositions (defined by x = Ga/(In+Ga)) were prepared via a three-stage method employing a vacuum evaporation system. The photocurrent from CIGS photocathode surfaces modified with CdS and Pt (Pt/CdS/CIGS) significantly increased along with x as a result of a reduction in the conduction band offset at the CIGS/CdS interface. Using an optimized aqueous electrolyte resulted in enhanced photocurrents of 28 and 18 mA cm^{-2} at 0 and 0.6 V$_{RHE}$, respectively, under simulated AM1.5G sunlight. A tandem-type PEC cell containing the newly developed CIGS photocathode and a BiVO$_4$ semi-transparent photoanode demonstrated stoichiometric hydrogen and oxygen evolution with a solar-to-hydrogen conversion efficiency of 3.7 % without the application of an external bias voltage.

Broader Context

The harvesting of solar energy in the form of chemical energy, such as by photoelectrochemical (PEC) water splitting to generate hydrogen and oxygen, is regarded as a vital aspect of addressing current energy and environmental issues. Photoelectrodes play an essential role in the PEC water splitting process, with n-type and p-type semiconductors typically acting as the photoanode and photocathode, respectively.

p-type semiconductor thin films based on copper chalcopyrite materials are one of the most promising photocathode material groups for hydrogen evolution. Among them, Cu(In,Ga)Se$_2$ was noted as a material with high half-cell solar-to-hydrogen conversion efficiency. However, considering the construction of PEC cell for overall water splitting, there is a requirement of further facilitation of photocurrent at around 0.6 V$_{RHE}$ which is the midpoint of the water potential window.

This paper presents new insights into highly efficient PEC hydrogen evolution via controlling the band off sets at CIGS/CdS interfaces, and, consequently, Cu(In,Ga)Se$_2$-based photocathode exhibited significantly enhanced solar energy conversion efficiency of 12.5% in hydrogen evolution from water and of 3.7% in overall water splitting with BiVO$_4$-based photoanode.

Introduction

Artificial photosynthesis for the production of commodity chemicals and fuels from carbon dioxide and water using solar energy has attracted significant attention as a viable approach to providing sustainable energy while protecting the environment.[1-4] The most important issue in this field is currently the development of photocatalytic systems capable of converting sunlight to various products with high energy efficiency.

Photoelectrochemical (PEC) water splitting represents a promising means of converting solar energy to hydrogen. Photoelectrodes play an essential role in this process, with n-type and p-type semiconductors typically acting as the photoanode and photocathode, respectively. Following the first report of water splitting using a TiO$_2$-based photoanode by Honda and Fujishima,[5,6] numerous photoelectrodes have been developed for the efficient utilization of sunlight. To date, quite a few highly efficient solar-driven water splitting devices have been reported,[7-9] the majority of which incorporate photoelectrodes assisted by photovoltaic cells or composed of multi-junction photovoltaic cells .

a. *Department of Chemical System Engineering, The University of Tokyo, 7-3-1 Hongo, Bunkyo-ku, Tokyo 113-8656, Japan. E-mail: domen@chemsys.t.u-tokyo.ac.jp; Fax: +81 3 5841 8838; Tel: +81 3 5841 1148*
b. *Frontier Core-Technology Laboratory, FujiFilm Corporation, 577 Ushijima, Kaisei-Machi, Ashigarakami-gun, Kanagawa 258-8577, Japan*
c. *PRESTO-JST, 7-3-1 Hongo, Bunkyo-ku, Tokyo 113-8656, Japan*
d. *Japan Technological Research Association of Artificial Photosynthetic Chemical Process (ARPChem), 7-3-1 Hongo, Bunkyo-ku, Tokyo 113-8656, Japan*

Our own groups has focused on fabricating simpler and more cost-effective photoelectrochemical systems. Our designs for water photo-splitting devices consist solely of a hydrogen evolution photocathode and an oxygen evolution photoanode, without the requirement for an external electric power supply. Based on this approach, we continue to develop new materials capable of absorbing visible light, as well as catalysts for hydrogen/oxygen evolution, and novel designs for the microscopic structures of photoelectrodes.

Chalcogenides are among the most promising photoelectrode materials, owing to their long absorption edge wavelengths combined with band structures well-suited to the water splitting reaction. Among these, $CuGaSe_2$,[10,11] $CuInS_2$,[12-14] $(ZnSe)_{0.85}(CuIn_{0.7}Ga_{0.7}Se_2)_{0.15}$[15] and $CuIn_{1-x}Ga_xSe_2$ (CIGS),[16,17] have absorption edge wavelengths of 750, 800, 900 and approximately 1200 nm, respectively. These materials exhibit remarkable properties as photocathodes. It should be noted that CIGS-based thin film prepared on 1 x 1 m substrate is already established for solar cells, and, thus, the thin film photoelectrodes based on these chalcogenides are possible to develop for large area.

In contrast to chalcogenide photocathodes, oxide and (oxy)nitride photoanodes have relatively short absorption edge wavelengths of less than 800 nm. For this reason, tandem-type PEC cells consisting of a top photoanode made of an oxide or (oxy)nitride and a bottom photocathode made of a chalcogenide are more likely to exhibit efficient water splitting. In the present study, we demonstrate water splitting by a tandem-type PEC cell composed of a $BiVO_4$-based semitransparent photoanode and a newly developed $CuIn_{1-x}Ga_xSe_2$ (CIGS)-based photocathode. Kumagai et al. applied a CIGS-based photocathode in which x (= Ga/(In+Ga)) was 0.3 to water reduction, and obtained a onset potential of cathodic photocurrent of more than 0.6 V_{RHE} together with a half-cell solar-to-hydrogen conversion efficiency (HC-STH) of 8.5% at 0.38 V_{RHE} through optimization of the electrolyte and surface.[17] Our group recently confirmed that a CIGS-based photocathode can generate 36 mA cm^{-2} at 0 V_{RHE} (see Figure S4 in the Supporting Information (SI)) However, the photocurrent generated by this device at high potentials was insufficient to drive water splitting efficiently when combined with a $BiVO_4$-based photoanode.[13] As such, there is a requirement to further improve the CIGS-based photocathode. In the present work, we assessed the effect of the x value on the PEC properties of CIGS. In addition, we demonstrated overall water splitting under simulated sunlight using a tandem-type PEC cell incorporating our newly developed CIGS-based photocathode, a $BiVO_4$-based photoanode and an optimized electrolyte.
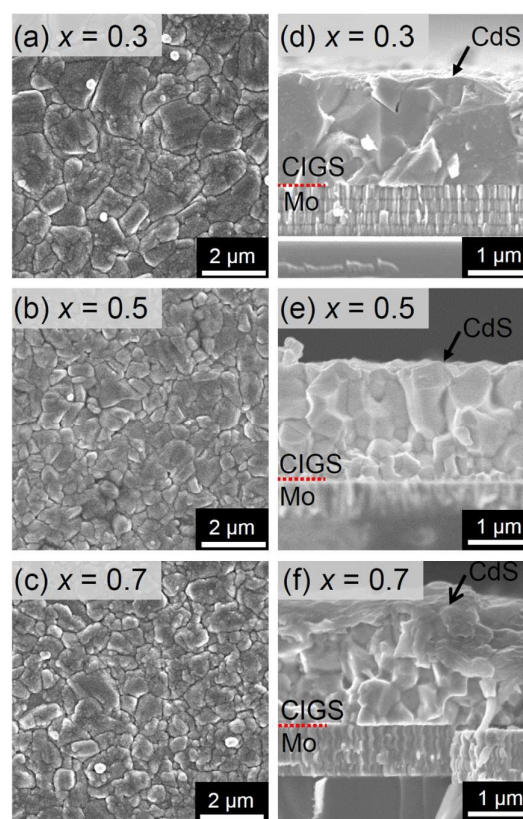
Results and discussion

Figure 1 (a-c) Top view and (d-f) cross-sectional SEM images of CdS/CIGS specimens having x (= Ga/(In+Ga)) values of 0.3, 0.5 and 0.7.

All CIGS films were deposited on Mo-coated soda-lime glass (SLG) plates using a multiple source vacuum evaporation system via a three-stage method,[18,19] as described in the Experimental section. The nominal atomic composition (x = Ga/(In+Ga)) of each specimen was determined by elemental analysis using inductively coupled plasma atomic emission spectroscopy (ICP-AES).

Figure 1 shows top-view and cross-sectional scanning electron microscopy (SEM) images of CIGS thin films following surface modification with CdS (CdS/CIGS) at x = 0.3, 0.5 and 0.7. These images demonstrate that the structural features of the films were modified by varying x. The CIGS films having x values from 0 to 0.5 were primarily composed of monolithic columnar grains bridging along the thickness direction. This morphology tends to promote electric conductivity and would therefore be expected to contribute to the efficient utilization of photoexcited carriers during the PEC reaction. In contrast, at x values greater than 0.5, the films were made of small grains with irregular shapes. The grain boundaries in such films could act as recombination sites for photoexcited carriers and may also increase the series resistance of the photoelectrode.[20]
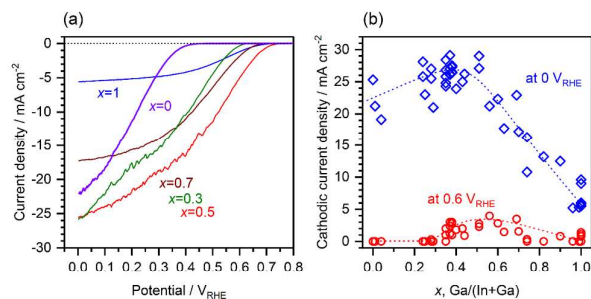
Figure 2 (a) Current-potential plots and (b) photocurrent values at 0 and 0.6 V_{RHE} for Pt/CdS/CIGS specimens having x = 0 to 1 under simulated AM1.5G sunlight, using 0.5 M Na_2SO_4 + 0.25 M Na_2HPO_4 + 0.25 M NaH_2PO_4 (aq.) adjusted to pH 6.8 with NaOH as the electrolyte. The applied potential was scanned at +20 mV s^{-1}.

These structural variations with composition can possibly be attributed to the different melting points of $CuGaSe_2$ (1070 °C) and $CuInSe_2$ (986 °C). The thickness of the CIGS layers in these SEM images ranges from 1.5 to 2 μm, while the CdS layer was found to be approximately 70 nm thick. X-ray diffraction (XRD) patterns were obtained for CIGS samples having x = 0 to 1 (Figure S1). The intense diffraction peaks in these patterns indicate a high degree of crystallinity, while the variations in the diffraction angles reflect a decrease in the lattice constants as x increases. No impurity phases were apparent for any x value. A secondary ion mass spectroscopy (SIMS) analysis of a typical CIGS film (Figure S2) produced a clear double-peaked profile, with a minimum local Ga/(In+Ga) ratio that was less than the nominal x value near the top surface. At the surfaces of both sides, the local Ga/(In+Ga) values were higher than the nominal x value.

CdS/CIGS/Mo photocathodes with various x values and modified with a Pt catalyst for hydrogen evolution (Pt/CdS/CIGS/Mo) were subjected to photoelectrochemical tests. Figure 2a shows current-potential curves acquired from these devices under simulated AM1.5G irradiation in an aqueous electrolyte containing 0.5 M Na_2SO_4 + 0.25 M Na_2HPO_4 + 0.25 M NaH_2PO_4 and adjusted to pH 6.8 with NaOH. Additional photocathodes were assessed to determine the photocurrent density at 0 V_{RHE} (the nominal potential for H_2 evolution), and at 0.6 V_{RHE} (the midpoint of the water potential window), and the results are shown in Figure 2b. It should be noted that the expected working potential for a PEC cell intended for overall water splitting and consisting of a photocathode and photoanode should be approximately 0.6 V_{RHE}. The series resistance of CIGS based photocathodes increase with composition, x = Ga/(In+Ga), at x >0.5 significantly because of decreased grain size, shown Figure S10 and Table S6.

Figure 2b demonstrates that the photocurrent at 0 V_{RHE} was almost constant for x = 0 to 0.5, but decreased at x above 0.5. At 0.6 V_{RHE}, the maximum photocurrent was obtained at x = 0.5 to 0.6. These photocurrent is, of course, closely related to the onset potential, where the hydrogen evolution
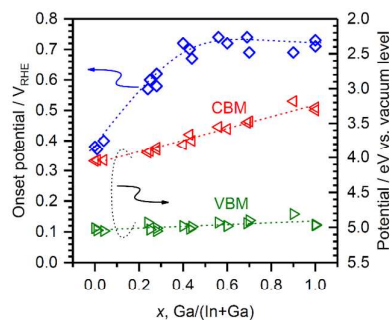

Figure 3 Onset potentials obtained from current-potential plots for Pt/CdS/CIGS photocathodes under simulated sunlight in 0.5 M Na_2SO_4 + 0.25 M Na_2HPO_4 + 0.25 M NaH_2PO_4 (aq.) adjusted to pH 6.8 with NaOH and the band edge potentials of CIGS thin films as functions of x (= Ga/(In+Ga)), as estimated from PESA and band gap data.

photocurrent falls to zero. Figure 3 shows the onset potentials for photocathodes with various x values made to the same specifications as those in Figure 2. Here, x-axis intercept showing 0 mA cm^{-2} was defined to be onset potential in the case of continuous irradiation. The onset potential is seen to increase monotonically in the range x = 0 to 0.4 and then plateaus, with a maximum of 0.75 V_{RHE}. A higher hydrogen evolution photocurrent onset potential is preferable in the case of dual-photoelectrode water splitting devices. On the basis of these experimental data, the CIGS photocathode with the highest performance in terms of the hydrogen evolution photocurrent is that for which x = 0.5.

To determine the association between the band structure of the CIGS films and the PEC properties, the valence band maximum (VBM) and conduction band minimum (CBM) potentials were investigated for various x values. The VBM potentials were determined by photoemission yield spectroscopy in air (PESA), while the band gap energy values were estimated using ultraviolet-visible (UV-vis) transmission spectroscopy (Figure S3). CBM potentials were obtained by adding these two values, and the results are shown in Figure 3. The VBM level was found to be constant for all x over the range of 0 to 1, whereas the CBM level increased almost proportionally to x.

The effect of the CIGS band structure on the PEC properties of the Pt/CdS/CIGS photocathode were assessed by generating band diagrams using the finite element method (FEM), employing the calculation method and parameters provided in the SI. The band diagrams at the solid-liquid interface with an applied potential of 0 V_{RHE} for CIGS specimens having x = 0.3 or 0.5 are presented in Figures 4a and 4b, while diagrams at 0.6 V_{RHE} for these same samples are shown in Figures 4c and 4d, respectively. It should be noted that the CBM offsets at the CIGS/CdS interfaces were found to be 0.34 V for x = 0.3 and 0.20 V for x = 0.5. The depth profile in Figure S2 demonstrates that the Ga content in the vicinity of the CIGS film surface was higher than the average throughout the entire film, as
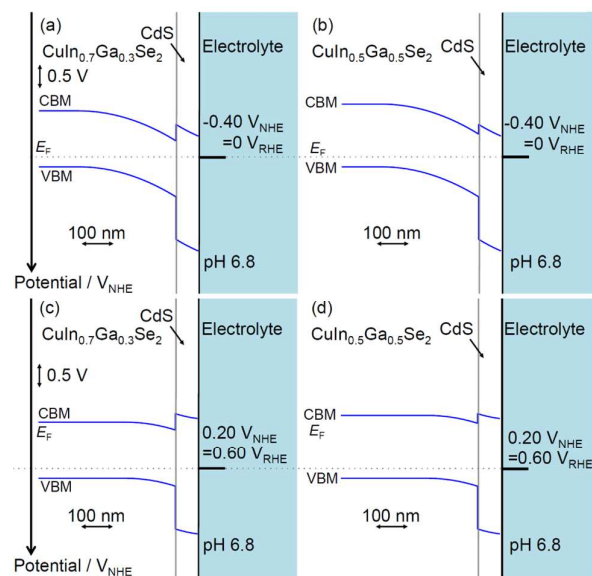
Figure 4 Calculated band diagrams for solid liquid interfaces of CdS/CIGS (*x* = 0.3 and 0.5) at applied potentials of (a and b) 0 V_{RHE} and (c and d) 0.6 V_{RHE}. (See SI for details regarding calculations and parameters.)

obtained by ICP analysis. Thus, the CBM offset between the CdS and CIGS could be smaller than anticipated. At an applied potential of 0 V_{RHE}, the upward CBM offsets are negligible as a result of the large built-in potentials for both photocathodes. Conversely, the upward CBM offset becomes significant at a relatively high applied potential of 0.6 V_{RHE}. In particular, the CBM potential for the CdS is higher than that for the CIGS (Figure 4c), and the considerable barrier resulting from the shallow CBM for the CdS suppresses the diffusion of photoexcited electrons from the CIGS to the hydrogen evolution sites. The decrease in the onset potential as *x* is increased occurs due to the increased CBM offset at the CIGS/CdS interface, and so higher *x* values should lead to higher onset potentials until the CBM for the CIGS equals that for the CdS. However, the CIGS grain size also decreased with increasing *x*, indicating increases in the series resistance and the number of recombination sites. Thus, the CIGS sample for which *x* = 0.5 showed the highest cathodic photocurrent because of the smaller CBM offset and larger grains. In the case of photovoltaic devices, a "spike-type" CBM offset has been found to be preferable, although in the present work this was found to be of no benefit due to the presence of the solid-liquid interface. It should be noted that the expected onset potential of the Pt/CdS/CIGS photocathode is equal to the Fermi level of CIGS, around 0.8-0.9 V_{RHE}, before the formation of band bending. Shallower CBM of CIGS can decrease loss related to the barrier caused by upward CBM offset while shallower CBM of CIGS has no contribution to the increase of expected onset potential. Thus, the onset potential of CIGS-based photocathode saturated at around *x* = 0.5.

As seen in Figure 2b, the optimized CIGS-based photocathode, Pt/CdS/CIGS with *x* = 0.5, generated photocurrent densities up

to 26 mA cm^{-2} at 0 V_{RHE} and 5.0 mA cm^{-2} at 0.6 V_{RHE} under simulated AM1.5G irradiation. Both these values are significantly higher than those obtained in a previous study.[17] However, further improvement is still possible. In Figure 2a, the absolute value of the photocurrent increases monotonically with decreasing potential, with no evidence of reaching an upper limit. Additionally, the fill factors for these current-potential curves were not satisfactory. This could be addressed by improving the electrical conductivity in each part of the electrochemical circuit, the most important of which would be the electrolyte solution.

For this reason, we surveyed various electrolytes by varying the chemical components and concentrations. The aqueous electrolytes examined consisted of sodium phosphate/sulfate buffers (pH 6.8), potassium phosphate/sulfate buffers (pH 6.8) and potassium borate buffers (pH 9.5). The conductivities of these solutions are provided in Tables S2, S3 and S4. Current-potential plots were acquired from a Pt/CdS/CIGS (*x* = 0.5) photocathode in these solutions under simulated AM1.5G irradiation (Figure S6). The 0.4 M K_2SO_4 + 0.4 M K_2HPO_4 + 0.4 M KH_2PO_4 solution (having the highest concentration) at a pH of 6.8 (adjusted using KOH) gave the highest conductivity (117 mS cm^{-1}) as well as the highest photocurrent, together with a good fill factor. It should be noted that both buffering ability and conductivity of an electrolyte are indispensable to obtain efficient PEC reaction as shown in Figure S8 in the ESI. Development of further functional electrolyte can be the important issue. In contrast, using the borate solution produced a photocurrent only half that obtained from the phosphate/sulfate buffer. The borate solutions were examined because they are known to be compatible with the $BiVO_4$ photoanode, as demonstrated by the tandem cell test described further on.

Figure 5a provides the current-potential curve acquired using a Pt/CdS/CIGS (*x* = 0.5) photocathode in the optimized electrolyte under chopped simulated AM1.5G sunlight. The photocurrent reached 28 mA cm^{-2} at 0 V_{RHE} and 18 mA cm^{-2} at
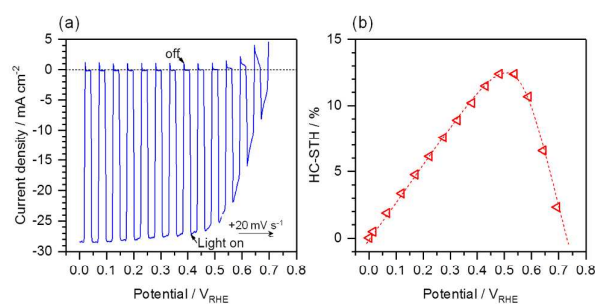

Figure 5 (a) Current-potential plot and (b) corresponding HC-STH data for a Pt/CdS/CIGS (*x* = 0.5) photocathode with the highest performance in 0.4 M K_2SO_4 + 0.4 M K_2HPO_4 + 0.4 M KH_2PO_4 (aq.) adjusted to pH 6.8 with KOH under chopped AM1.5G irradiation. The potential was swept at +20 mVs^{-1}.

0.6 V_{RHE}. In addition, the photocurrent density was almost

saturated at approximately 28 mA cm^{-2} below 0.4 V$_{RHE}$ such that the data plot plateaued, demonstrating a good square fill factor. Figure 5b was derived by calculating the HC-STH values
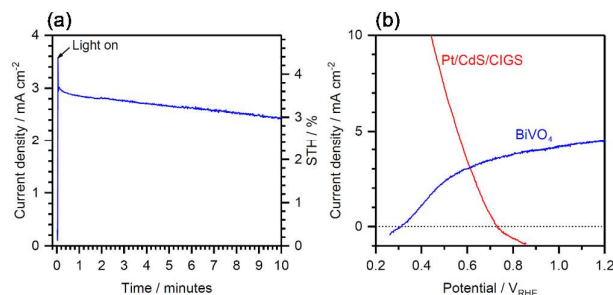

Figure 6 (a) Time course of the photocurrent and corresponding STH values for a tandem PEC cell composed of a BiVO$_4$-based top photoanode and a CIGS-based bottom photocathode under simulated AM1.5G sunlight and (b) current-potential plots for a CIGS-based photocathode and a BiVO$_4$-based photoanode used in the tandem PEC cell as acquired under continuous irradiation with simulated AM1.5G sunlight. The CIGS-based photocathode was measured under BiVO$_4$-based photoanode. Note that the photocathode data are plotted with the sign of the photocurrent inverted.

from Figure 5a. The HC-STH curve exhibits a maximum value of 12.5% at 0.53 V$_{RHE}$, and is higher than 10% at 0.35 to 0.6 V$_{RHE}$. These are the highest values yet reported for photocathodes (other than those based on single crystals) and are considerably higher than that previously reported for a CIGS-based photocathode.[21]

We assessed the performance of the optimized Pt/CdS/CIGS (*x* = 0.5) unit when assembled in a tandem cell for overall water splitting. For this purpose, a photoanode appropriate for oxygen evolution was necessary. This photoanode had to generate a positive photocurrent at a lower potential than the onset potential for the CIGS photocathode, with the highest possible photocurrent density. Among the photoanodes previously fabricated, those made from BiVO$_4$ have been found most suitable for use as photoanodes in terms of both electrochemical properties and availability.

A tandem cell with a (Ag, Cu)GaSe$_2$-based photocathode and a BiVO$_4$-based photoanode that takes advantage of the semitransparency of a BiVO$_4$-based photoanode prepared on a transparent substrate (indium tin oxide (ITO)) has been previously reported.[22] However, the STH value of this device was low (less than 1%), and so our aim in the present study was to improve this STH using our new CIGS formula. Nano-porous BiVO$_4$ films on transparent ITO substrates were first fabricated by Choi et al.[23,24] and later substantially improved by Kuang et al.[25,26]

Based on these prior studies, Fe and Ni were simultaneously loaded as oxygen evolution catalysts on a nano-worm BiVO$_4$ electrode. The PEC cell was arranged such that the catalyst sides of the CIGS and BiVO$_4$ electrodes faced one another, and

simulated AM1.5G sunlight was applied through the ITO substrate of the BiVO$_4$ electrode. In this arrangement, only the light transmitted through the BiVO$_4$ electrode was applied to the CIGS electrode.

When combining CIGS and BiVO$_4$, it is necessary to select an electrolyte that optimizes the performance of the CIGS from among those suitable for use with BiVO$_4$. As discussed above, 0.5 M K$_3$BO$_3$ adjusted to pH 9.5 with KOH has been shown to be optimal for BiVO$_4$[25,26,27,28] as a buffer solution, giving a relatively high electrical conductivity and compatibility with Fe-Ni catalysts.

Figure 6a shows the time course of the photocurrent generated by the dual photoelectrode cell over the first 10 min. The STH was 3.7% at 5 s immediately after the initial current spike and fell to 3.0% after 10 min. This decrease in the photocurrent can be attributed to an increase in the spatial pH gradient through the consumption of H$^+$ around the photocathode and generation of OH$^-$ around the photoanode. Figure 6b shows the current-potential curves obtained from a CIGS photocathode with a light acceptance area of 0.1 cm^2 and a BiVO$_4$ photoanode with the same area of 0.1 cm^2 measured independently in the solution described above. Tandem cells should generate the highest possible STH when the two electrodes have the same light acceptance areas and are exactly overlapped. Note that, in the graph shown in Figure 6b, the sign of the cathodic current is reversed. When the two curves cross each other at a non-zero photocurrent, hydrogen and oxygen are evolved from water over the photocathode and photoanode, respectively. The working potential for the electrodes appears to be approximately 0.6 V$_{RHE}$, at which point the photocurrent will be approximately 3 mA cm^{-2}. This photocurrent derived from the current-potential curve matches the initial photocurrent observed in Figure 6b. Without supplying an external voltage, this type of tandem cell (representing a stand-alone overall water splitting device) evolves hydrogen and oxygen at stoichiometric rates with 100% Faradaic efficiency as long as it is irradiated with simulated sunlight (Figure S7).

Conclusions

A novel Pt/CdS/CIGS photocathode having a specific compositional ratio in the CIGS layer showed a remarkable degree of hydrogen evolution from water, giving an HC-STH of 12.5%. A band structure analysis based on PESA and UV-vis data determined that the VBM potential remained constant as *x* (= Ga/(In+Ga)) was varied, whereas the CBM potential increased nearly proportionally to *x*. The photocurrent density measured under AM1.5 G simulated sunlight exhibited a monotonic increase in onset potential in the range *x* = 0 to 0.4, but plateaued in the range *x* = 0.4 to 1.0, with a maximum of 0.75 V$_{RHE}$. The band diagrams obtained through FEM calculations elucidated the significance of the *x* value in determining the CBM offset, which in turn can affect the onset potential for the cathodic photocurrent. As such, the monotonic increase in the onset potential from *x* = 0 to 0.4 is attributed to a corresponding decrease in the VBM offset. An *x*

value of 0.5 is believed to be optimal considering the variation in the compositional ratio at the CIGS/CdS interface and the significance of the upward CBM offset. The use of an aqueous 0.4 M K_2SO_4 + 0.4 M K_2HPO_4 + 0.4 M KH_2PO_4 solution adjusted to pH 6.8 as an electrolyte resulted in the largest photocurrent from the newly developed Pt/CdS/CIGS photocathode. Using this device, the highest conductivity of 117 mS cm^{-1}, a significantly improved HC-STH value of 12.5% at 0.53 V_{RHE} and values higher than 10% at 0.35 to 0.6 V_{RHE} were achieved. The HC-STH of 12.5% is the highest efficiency yet reported for a photocathode among the non-single crystal-based, [21] and non-buried junction-based ones.

A tandem-type PEC cell incorporating the newly-developed CIGS photocathode and a semi-transparent $BiVO_4$ photoanode demonstrated stoichiometric hydrogen and oxygen evolution with an STH of 3.7% without the application of an external voltage. Furthermore, since this STH is limited by the anode performance, it should be possible to obtain STH values above 10% when employing a more efficient photoanode in future iterations of this cell.

Experimental

Preparation of the photoelectrodes

A Mo back contact layer was deposited onto SLG by DC magnetron sputtering. A CIGS light-absorber layer was subsequently grown on this Mo layer using a three-stage method in conjunction with a multiple source vacuum evaporation system.[18,19] High purity (>5 N) elemental Cu, In, Ga and Se were used as the evaporation sources and the substrate temperatures in the first, second and third stages were 400, 520 and 520 °C, respectively. This three-stage method was intended to generate a so-called double-graded structure. The In/Ga ratio was adjusted by controlling the evaporation rates of the In and Ga sources, and the overall compositional ratio (x = Ga/(In+Ga)) in the film was verified by ICP elemental analysis, as described below. A CdS buffer layer was formed on the CIGS films by chemical bath deposition (CBD) using an aqueous 1.5 mM $CdSO_4$ + 1.5 M NH_4OH + 7.5 mM thiourea solution at 70 °C for 40 min.[29] The Mo, CIGS and CdS film thicknesses were 600 nm, 2 μm and 70 nm, respectively. Finally, Pt particles were deposited on the CdS/CIGS films as a hydrogen evolution catalyst by DC magnetron sputtering using a Pt target.

Semi-transparent $BiVO_4$ photoanodes were prepared according to a previously reported method.[24,26] $BiVO_4$ was synthesized by electrochemically depositing a BiOI precursor on a commercially-available glass plate covered with ITO (GEOMATEC, sheet resistivity: 5 Ω/square). A dimethyl sulfoxide (DMSO) solution of vanadyl acetylacetonate $(VO(acac)_2)$ was subsequently drop cast onto the BiOI precursor layer and heated at 450 °C for 1 h in air. The Fe/Ni oxide catalyst was electro-deposited from a mixture made by adding 0.01 M nickel sulfate (II) in water (80 μL) and 0.01 M iron sulfate (II) (800 μL) to 200 mL of a 0.5 M K_3BO_3 solution pre-adjusted to pH 9.0 with KOH. While in this solution, the

$BiVO_4$ electrode was held at -0.160 V_{RHE} and Fe and Ni were electrodeposited on the $BiVO_4$ surface for 15 min.

Material characterization

XRD (CuKα radiation, SmartLab, Rigaku) was employed for structural analysis of the CIGS films. The overall elementary analysis of the CIGS films was performed by ICP-AES (8100, Shimadzu) after liquefaction by molten-salt decomposition. The composition gradients in the thickness direction of the CIGS films were determined using SIMS (PHI ADEPT-1010, Ulvac-Phi). Band gaps were measured by UV-vis spectroscopy (V-770, Jasco). VBM levels were estimated from the ionization potentials obtained from PESA analyses of the sample surfaces (AC-3, Riken Keiki), and these values in turn were employed to determine the CBM levels. Scanning electron microscopy (SEM) was performed with a field-emission electron source (SU8020, Hitachi). Transmission electron microscopy (TEM) images were obtained using a JEM-ARM200F instrument (JEOL) capable of analysis with atomic resolution.

Photoelectrochemical measurements

A typical three electrode evaluation system was used for PEC measurement of the CIGS electrodes.[23,30] A Pt wire and Ag/AgCl in a saturated aqueous solution of KCl were used as the counter and reference electrodes, respectively. Prior to each trial, dissolved oxygen in the electrolytic solution was removed by bubbling with argon gas. A solar simulator (XES-70S1, SAN-EI Electric) applying AM1.5G irradiation at 100 mWcm^{-2} was employed as the light source, with stray light other than that from the solar simulator blocked by dark curtains. Photocurrents were acquired at a scanning rate of 20 mVs^{-1} using a potentiostat (HZ-7000, Hokuto), and the potentials obtained from these trials were converted to values against a reversible hydrogen electrode (RHE, $E_{RHE} = E_{Ag/AgCl}$ + 0.059 pH + 0.199).[31] The quantities of gaseous hydrogen and oxygen evolved by the overall water splitting were quantified by gas chromatography (3000 micro GC, INFICON). The hypothetical HC-STH values were calculated from the equation HC-STH = $I_{ph} \times (E_{RHE} - E_{H+/H2})/P_{sun} \times 100\%$, where I_{ph} is the photocurrent density obtained under an applied bias of E_{RHE}, $E_{H+/H2}$ is 0 V_{RHE} and P_{sun} is 100 mWcm^{-2}.

Conflicts of interest

There are no conflicts to declare.

Acknowledgements

Notes and references

1   M. Gratzel, *Cattech*, 1999, **3**, 3-17.
2   T. Arai, S. Sato, T. Morikawa, *Energy Environ. Sci.*, 2015, **8**, 1998-2002.
3   C. Jiang, S. J. A. Moniz, A. Wang, T. Zhang, J. Tang, *Chem. Soc. Rev.*, 2017, **46**, 4645-4660.
4   Z. Li, W. Luo, M. Zhang, J. Feng and Z. Zou, *Energy Environ. Sci.,* 2013, **6**, 347-370.
5   A. Fujishima and K. Honda, *Bull. Chem. Soc. Jpn.,* 1971, **44**, 1148–1150.
6   A. Fujishima and K. Honda, *Nature,* 1972, **238**, 37–38.
7   M. M. May, H-J. Lewerenz, D. Lackner, F. Dimroth, *Nat. Commun.* 2015, **6**, 8286 (1-7)
8   F. Urbain, V. Smirnov, J-P. Becker, A. Lambertz, F. Yang, J. Ziegler, B. Kaiser, W. Jaegermann, U. Rau and F. Finger, *Energy Environ. Sci.*, 2016,9, 145-154.77.
9   J. Luo, J. -H. Im, M. T. Mayer, M. Schreier, M. K. Nazeeruddin, N. -G. Park, S. D. Tilley, H. J. Fan, M. Grätzel, *Science*, 2014, **345**, 1593-1596.
10 M. Moriya, T. Minegishi, H. Kumagai, M. Katayama, J. Kubota and K. Domen, *J. Am. Chem. Soc.,* 2013, **135**, 3733–3735.
11 H. Kumagai, T. Minegishi, Y. Moriya, J. Kubota and K. Domen, *J. Phys. Chem. C,* 2014, **118**, 16386–16392.
12 S. Ikeda, T. Nakamura, S. M. Lee, T. Yagi, T. Harada, T. Minegishi and M. Matsumura, *ChemSusChem,* 2011, **4**, 262–268.
13 J. Zhao, T. Minegishi, L. Zhang, M. Zhong, Gunawan, M. Nakabayashi, G. Ma, T. Hisatomi, M. Katayama, S. Ikeda, N. Shibata, T. Yamada and K. Domen, *Angew. Chem., Int. Ed.,* 2014, **53**, 11808–11812.
14 Gunawan, W. Septina, S. Ikeda, T. Harada, T. Minegishi, K. Domen and M. Matsumura, *Chem. Commun.,* 2014, 50, 8941–8943.
15 H. Kaneko, T. Minegishi, M. Nakabayashi, N. Shibata, Y. Kuang, T. Yamada, K. Domen, *Adv. Funct. Mater,.* 2016, **26**, 4570–4577.
16 D. Yokoyama, T. Minegishi, K. Maeda, M. Katayama, J. Kubota, A. Yamada, M. Konagai and K. Domen, *Electrochem. Commun.,* 2010, **12**, 851–853.
17 H. Kumagai, T. Minegishi, N. Sato, T. Yamada, J. Kubota, K. Domen, *J. Mater. Chem. A,* 2015, **3**, 8300-8307.
18 A. M. Gabor, J. R. Tuttle, D. S. Albin, M. A. Contreras, R. Noufi, A. M. Hermann, *Appl. Phys. Lett.,* 1994, **65**, 198-200.
19 J. R. Tuttle, M. Contreras, M. H. Bode, D. Niles, D. S. Albin, R. Matson, A. M. Gabor, A. Tennant, A. Duda, R. Noufi, *J. Appl. Phys.,* 1995, **77**, 153-161.
20 Idris B, Rafik Z, Kamal D, Abdessalam B, Faouzi G, *Renewable Energy Congress (IREC), 2015 6th International,* 2015, **24-26**, 1-5.
21 M. H. Lee, K. Takei, J. Zhang, R. Kapadia, M. Zheng, Y.-Z. Chen, J. Nah, T. S. Matthews, Y.-L. Chueh, J. W. Ager and A. Javey, *Angew. Chem., Int. Ed.,* 2012, **51**, 10760–10764.
22 J. Kim, H. Kaneko, T. Minegishi, J. Kubota, K. Domen, J. Lee, *ChemSusChem*, 2016, **9**, 61–66.
23 M.-W. Kim, H. Yoon, T. Y. Ohm, M. G. Mali, S. K. Choi, H. Park, S. S. A. Deyab, D. C. Lim, S. Ahn, S. S. Yoon, *J. Alloys and Compounds*, 2017, **692**, 294-300.
24 T. W. Kim, K. -S. Choi, *Science*, **2014**, *343*, 990-994
25 Y. Kuang, Q. Jia, G. Ma, T. Hisatomi, T. Minegishi, H. Nishiyama, M. Nakabayashi, N. Shibata, T. Yamada, A. Kudo, K. Domen, *Nat. Energ.* **2016**, *2*, 16191 (1-9)
26 Y. Kuang, Q. Jia, H. Nishiyama, T. Yamada, A. Kudo, K. Domen, *Adv. Energy Mater.* **2016**, *6*, 1501645 (1-7)
27 S. K. Choi, W. Choi, H. Park, *Phys. Chem. Chem. Phys.*, 2013, **15**, 6499-6507.
28 C. Ding, J. Shi, D. Wang, Z. Wang, N. Wang, G. Liu, F. Xiong, C. Li, *Phys. Chem. Chem. Phys.*, 2013, **15**, 4589-4595
29 K. Ramanathan, F. S. Hasoon, S. Smith, D. L. Young, M. A. Contreras, P. K. Johnson, A. O. Pudov, J. R. Sites, *J. Phys. Chem. Solids,* 2003, **64**, 1495-1498.
30 T. J. Jacobsson, C. P. Bjorkman, M. Edoff, T. Edvinsson, *Int. J. Hydrogen energy*, 2013, 38, 15027-15035.
31 Z. Chen, T. F. Jaramillo, T. G. Deutsch, A. K. Shwarsctein, A. J. Forman, N. Gaillard, R. Garland, K. Takanabe, C. Heske, M. Sunkara, E. W. McFarland, K. Domen, E. L. Miller, J. A. Turner, H. N. Dinh, *J. Mat. Res. ,* 2010, 25, 3-16.